

# Lateral heterostructures of hexagonal boron nitride and graphene: BCN alloy formation and microstructuring mechanism

Marin Petrović,<sup>1,2,\*</sup> Michael Horn-von Hoegen,<sup>1</sup> and Frank-J. Meyer zu Heringdorf<sup>1</sup>

<sup>1</sup>*Faculty of Physics and CENIDE, University of Duisburg-Essen, Lotharstr. 1, D-47057 Duisburg, Germany*

<sup>2</sup>*Center of Excellence for Advanced Materials and Sensing Devices, Institute of Physics, Bijenička cesta 46, HR-10000 Zagreb, Croatia*

Integration of individual two-dimensional materials into heterostructures is a crucial step which enables development of new and technologically interesting functional systems of reduced dimensionality. Here, well-defined lateral heterostructures of hexagonal boron nitride and graphene are synthesized on Ir(111) by performing sequential chemical vapor deposition from borazine and ethylene in ultra-high vacuum. Low-energy electron microscopy (LEEM) and selected-area electron diffraction ( $\mu$ -LEED) show that the heterostructures do not consist only of hexagonal boron nitride (an insulator) and graphene (a conductor), but that also a 2D alloy made up of B, C, and N atoms (a semiconductor) is formed. Composition and spatial extension of the alloy can be tuned by controlling the parameters of the synthesis. A new method for in situ fabrication of micro and nanostructures based on decomposition of hexagonal boron nitride is experimentally demonstrated and modeled analytically, which establishes a new route for production of BCN and graphene elements of various shapes. In this way, atomically-thin conducting and semiconducting components can be fabricated, serving as a basis for manufacturing more complex devices.

## I. INTRODUCTION

Two-dimensional materials (2DMs) have invoked significant interest in the scientific community due to their exciting novel properties and possible applications. Despite extensive investigation, incorporation of 2DMs into new, more complex structures remains a challenge. One attractive route for 2DMs integration is fabrication of heterostructures, where layers of different materials are stacked one on top of another or side by side [1]. In this way, constituent materials are exploited for obtaining thin and flexible systems with new functionalities and improved properties. For example, heterostructures of graphene (Gr), hexagonal boron nitride (hBN) and transition-metal dichalcogenides can be used for fabrication of advanced transistors, diodes and photovoltaic devices [2–5].

In the case of lateral heterostructures, a lot of attention has been given to joint monolayers of Gr and hBN [6], since these two materials both have hexagonal lattices with similar lattice parameters, but differ substantially in terms of their electronic structure. While Gr is an excellent conductor with high carrier mobility [7], hBN is an insulator with an electronic gap of  $\sim 6$  eV [8]. These properties make hBN-Gr lateral heterostructures very appealing for construction of atomically thin electronics. However, it is still demanding to fabricate these heterostructures as desired. One direction of their production is the use of focused ion beam and lithography (in combination with material regrowth) [9–11], which are widely used for post-growth tailoring of the 2DMs. These techniques represent straightforward tools for fabrication of hBN-Gr interfaces of various shapes, but they

require ex situ manipulation of the 2DMs, resulting in a decreased quality of the final structures. Also, control over the interface on the atomic scale (e.g., number of defects, edge type or material intermixing) is poor, which can impair functionality of future devices.

A common way to tackle these issues is by employing chemical vapor deposition (CVD), which often implies epitaxial growth. For example, atomically sharp interfaces in hBN-Gr lateral heterostructures have been achieved on Rh(111), Ru(0001), Ir(111), Ni(111), and Cu foils [12–17]. However, heterostructures synthesized in such way were limited in terms of shape and size, and no real-time monitoring of their fabrication was possible in most cases. An exception is hBN-Gr synthesis on Ru(0001), where low-energy electron microscopy (LEEM) was used to uncover details of growth dynamics [12, 15]. In a general case, atomically sharp interfaces between hBN and Gr may not always be desirable and a certain level of mixing (i.e. 2D alloying) can be useful. In particular, a material consisting of hexagonally arranged C, B and N atoms (hBCN, without implication of exact stoichiometry) was theoretically predicted to be semiconducting with a bandgap tunable by altering the C:(B,N) ratio [18–22]. These predictions were experimentally confirmed for the case of hBC<sub>2</sub>N where a direct bandgap of  $\approx 2$  eV was found [23, 24], which makes this alloyed material very interesting for optoelectronic applications. Therefore, hBCN holds a unique place in the family of 2D materials, and its investigation is well-justified.

Here, we study hBN-Gr lateral heterostructures on Ir(111). By using LEEM, the synthesis was monitored in real-time, and details of the hBN-Gr boundary were investigated by low-energy electron diffraction (LEED). In addition, we introduce a technique which effectively produces various micron-sized elements of graphene and hBCN alloy out of heterostructures, establishing in such way a new route for microstructuring of 2DMs.

\* mpetrovic@ifs.hr

## II. EXPERIMENTAL METHODS

Growth of hBN-Gr heterostructures was conducted on a Ir(111) surface (single-crystal, Mateck) in an ultra-high vacuum (UHV) setup dedicated to LEEM and photoemission electron microscopy (PEEM) at the University of Duisburg-Essen. The Ir crystal was cleaned by Ar<sup>+</sup> sputtering at 2 keV followed by several cycles of heating in oxygen at 1170 K and annealing at 1470 K. Sequential CVDs from borazine (B<sub>3</sub>H<sub>6</sub>N<sub>3</sub>) and ethylene (C<sub>2</sub>H<sub>4</sub>) were used for the synthesis of hBN-Gr heterostructures. Experimental parameters used in the synthesis and microstructuring process are discussed in the context of the specific experiments below. The sample temperature was measured with an infrared pyrometer. Borazine and ethylene were dosed into the UHV chamber through leak-valves. Borazine was kept in a Peltier cooler to prevent its degradation. Prior to each hBN synthesis, the borazine inlet line was evacuated to remove any decomposition residues.

LEEM, LEED and PEEM measurements were carried out in situ with an Elmitec SPE-LEEM III microscope with a spatial resolution of  $\sim 10$  nm. A mercury discharge lamp was used for sample illumination during PEEM. The bright field (BF) mode was used for LEEM imaging, where the contrast aperture allowed passage of the central (0,0) spot and the first-order moiré spots into the imaging column of the microscope. Consequently, areas on the sample exhibiting even the smallest differences in the moiré pattern can be imaged with distinctive contrast in real space, and this will be very useful for visualization of different regions of hBN-Gr heterostructures. The same effect has been used for identification of local lattice constant changes of Gr on Ir(111) during wrinkling [25]. In electron diffraction experiments, only a small micron-sized circular area of the sample surface ( $d \approx 0.5$   $\mu\text{m}$ ) was illuminated with an electron beam, thus enabling micro-LEED ( $\mu$ -LEED) analysis.

## III. RESULTS

### A. Heterostructure Growth and Composition

The formation of hBN-Gr lateral heterostructures is shown in Figure 1 in a sequence of LEEM images (see also Supplementary Movie 1). First, well-defined hBN islands are grown as shown in Figure 1(a) by exposing the Ir surface at 1170 K to  $10^{-8}$  mbar of borazine. As reported previously, triangular and trapezoidal hBN islands form on the surface, with the short base of the trapezoidal islands oriented in the step-up direction of the Ir surface [26]. After stopping the borazine dosing and allowing the pressure to recover, ethylene was introduced into the UHV chamber as a precursor for Gr growth with a pressure of  $10^{-8}$  mbar, while keeping the sample temperature at 1170 K the entire time. This resulted in the formation of the new material exclusively at

the edges of preexisting hBN islands, as shown in Figure 1(b), whose structure and composition will be analyzed later in the text. If the ethylene pressure during CVD was raised to  $\sim 10^{-7}$  mbar, additional Gr nucleation on bare Ir areas was observed. Heterostructure growth in the vertical direction is not possible due to the inertness (i.e., lack of catalytic activity) of hBN. Further exposure to ethylene results in roughly isotropic expansion of the heterostructure perimeter, as is visible in Figure 1(c) and (d). However, the new material growing attached to hBN exhibits variations in electron reflectivity, indicating that the material is not purely Gr, as might be expected during dosage of solely ethylene. PEEM images of heterostructures also show similar variations of intensity, indicating alteration of the electronic properties across the heterostructure (see Supplementary Figure S1). In all our LEEM data, bright regions always form in the step-down direction of the Ir surface. Also, streaks of dark regions, often confined by the Ir step edges, are regularly found embedded in the bright regions [see white arrow in Figure 1(d)]. These findings indicate that the Ir surface step morphology is decisive for the growth of the new material.

The concentration of adsorbed species on the Ir surface during heterostructure formation was determined by monitoring LEEM reflectivity in the vicinity of the growing islands. The concentration of adsorbates  $c_{\text{ad}}(t)$  is proportional to the LEEM reflectivity decrease  $I_0 - I(t)$ , where  $I_0$  is reflectivity of the surface free of any adsorbates [12, 27]. Normalized reflectivity change  $[I_0 - I(t)]/I_0 \propto c_{\text{ad}}(t)$  is represented in Figure 1(e) by red circles, with the corresponding data taken from the area indicated with a red rectangle in the inset. The concentration of the adsorbates increases monotonically upon borazine introduction into the UHV chamber until the borazine is turned off [orange region in Figure 1(e)], with a small drop at  $t \approx 75$  s which we relate to the onset of hBN nucleation [27]. It is crucial to note that there are still adsorbate species present on the Ir surface even after the borazine supply has been switched off and before the ethylene is introduced into the chamber at  $t \approx 225$  s [green region in Figure 1(e)]. The concentration of all adsorbed species increases rapidly until  $t \approx 275$  s when the formation of new material attached to hBN cores starts, which is visible in Figure 1(e) as a sharp onset of the concentration decrease. Because different adsorbates generally cause different reflectivity changes in LEEM, comparison of adsorbate concentrations during the course of heterostructure formation in Figure 1(e) cannot be done directly.

The reflectivity analysis suggests that during sequential CVD growth of hBN-Gr heterostructures, mixing of species originating from both borazine and ethylene takes place on the Ir surface and an alloy is formed. Further clear-cut evidence of this is found in experiments where the ethylene pressure was periodically modified during CVD between  $2 \times 10^{-8}$  and  $7 \times 10^{-8}$  mbar with a period of  $\sim 42$  s, thus varying the carbon supply during the syn-

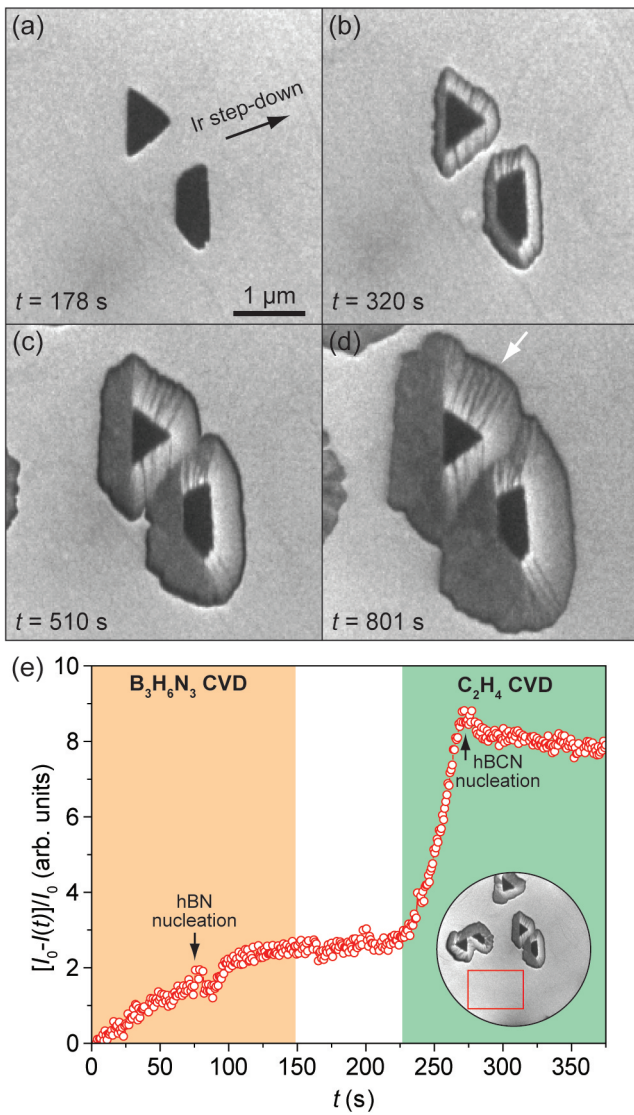


Figure 1. (a)-(d) A sequence of LEEM images showing the formation of hBN-Gr lateral heterostructures. In panel (a), two hBN islands are visible. In panels (b)-(d), new material (Gr and hBCN alloy) is growing from the edges of hBN islands. Time relative to the beginning of the borazine dosing is indicated in each panel.  $T_S = 1170$  K,  $E = 9$  eV. (d) Normalized change of electron reflectivity as a function of time. Data was extracted from the area indicated by a rectangle in the inset, in the vicinity of the heterostructures shown in (a)-(d). Orange and green shading indicate periods of borazine and ethylene CVD, respectively.

thesis. The resulting structure is shown in Figure 2(a), where hBN cores are surrounded by equidistant carbon-poor (high reflectivity contours) and carbon-rich (low reflectivity contours) regions. A cross-section taken from Figure 2(a) is shown in panel (b), where six minima corresponding to six consecutive ethylene pressure increases are superposed to exponentially decaying LEEM reflectivity (see also Supplementary Figure S2). Lateral extension of carbon-poor or carbon-rich regions can be tuned

by changing the duration of decreased or increased ethylene pressure in the course of the synthesis. For the heterostructures shown in Figure 2, average separation of the individual regions is less than  $0.2 \mu\text{m}$ .

If the sample is treated with oxygen between the borazine and ethylene CVD steps, the concentration of the leftover borazine species is significantly reduced. Consequently, pure hBN and Gr regions become better defined and the transition region between them becomes narrower (see Supplementary Figure S3). Another route for controlling the extent of the transition region is modification of the synthesis temperature, where lower temperatures produce narrower transition between hBN and Gr due to the lower concentration of leftover adsorbed borazine species (see Supplementary Figure S2). The same procedures for improving Gr-hBN interface are effective for heterostructures synthesized on Ru(0001) [12]. At this point we assume (and later on we will elucidate) that the mixed material is a hexagonal mesh composed of C, B and N, and hence we label it as hBCN.

The crystal structure of the hBN-Gr heterostructures was analyzed in detail by performing  $\mu$ -LEED. The area of the sample selected for this is shown in Figure 3(b) where two coalesced heterostructures are visible, similar as in Figure 1(d). The boundary between them is highlighted by the dashed line  $L_1$ . The edge towards uncovered Ir is marked by the dashed line  $L_2$ . The path of the  $\mu$ -LEED scan is marked by the horizontal dashed line  $L_3$ . Important information about the crystal structure was extracted from the analysis of the central region of the diffraction pattern where the moiré diffraction spots surrounding the (0,0) spot are located. Several characteristic diffraction patterns, originating from the areas marked in Figure 3(b) by yellow circles, are shown in Figure 3(d) (a complete  $\mu$ -LEED scan is given in the Supplementary Movie 2). Diffraction of the core hBN island (box 2) shows a clear pattern corresponding to hBN/Ir(111). The diffraction recorded at the edge of the heterostructure (box 5) exhibits the pattern which is associated with Gr/Ir(111). Between these two limiting cases, in the hBCN region the diffraction pattern shows significant variation of the moiré spots position and intensity (boxes 1, 3 and 4). To capture this variation in a systematic way, radial average and polar profile of the central part of the  $\mu$ -LEED scan were extracted from the Supplementary Movie 2 and are plotted in Figure 3(a) and (c), respectively. The radial average displays information about the distance of the moiré diffraction spots from the center of the Brillouin zone (i.e., their  $k$ -value), and the polar profile provides information about the angular distribution of the moiré spots. Calibration of the  $k$ -space was done by measuring the first-order Ir(111) diffraction spots ( $k_{\text{Ir}}, 2\pi/2.715 \text{ \AA}$  [28]).

Small changes in the rotation or lattice size of epitaxial 2D materials are effectively magnified by an order of magnitude via moiré spots re-positioning [28]. This effect is exploited in the following, where we focus on the right one of the two hBN-Gr heterostructures from Figure 3(b).

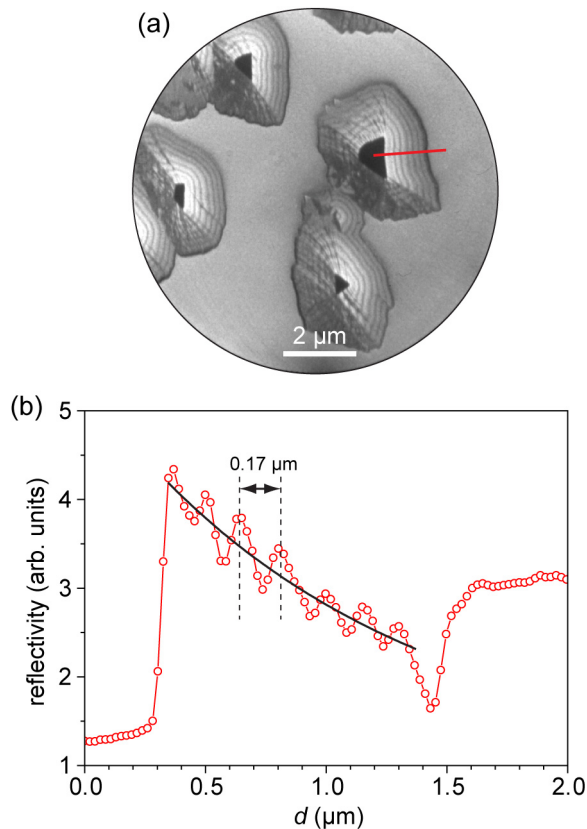


Figure 2. (a) LEEM image of the hBN-Gr heterostructure with modulated carbon content [i.e., C:(B,N) ratio] in the region of the hBCN alloy, visible as equidistant contours (dark contours correspond to carbon-rich regions, bright contours to carbon-poor regions).  $T_S = 1170$  K,  $E = 9$  eV. (b) Cross-section taken from panel (a) as indicated by a red line. Carbon-rich and carbon-poor regions are identified as minima and maxima in LEEM reflectivity that are superposed to an exponentially decaying background (black line). Red lines are guides to the eye.

Saturated intensity at the bottom of the Figure 3(a) corresponds to the (0,0) spot, which is present throughout the  $\mu$ -LEED scan (including the area of bare Ir). The second most intense peak corresponds to the first-order moiré diffraction spots. Evidently, the distance of the moiré peak from the (0,0) spot changes across the scan, as well as its intensity. The  $k$ -values of the Gr ( $k_{m,Gr}$ ,  $2\pi/25.3\text{\AA}$ ) and hBN ( $k_{m,hBN}$ ,  $2\pi/29.1\text{\AA}$ ) moiré structures on Ir(111) [28, 29] are marked by horizontal dotted lines. The moiré peak shifts between these two values as a function of position within the heterostructure. Directly at the hBN core, the first-order moiré diffraction spots have a  $k$ -value corresponding to the hBN/Ir(111), in agreement with a clear and sharp diffraction pattern shown in box 2 of Figure 3(d). In a similar manner, material located at the edge of the heterostructure is characterized by a  $k$ -value of Gr/Ir(111) and shows a diffraction pattern characteristic for that system [box 5 of Figure 3(d)]. When scanning from the hBN to the Gr region (in the

step-down direction of the Ir surface), the  $k$ -value of the moiré structure gradually increases, i.e., the real space lattice constant of hBCN decreases. Also, the intensity of the moiré diffraction spots drops suddenly after leaving the hBN core [cf. box 3 of Figure 3(d)], and gradually increases as the edge of the heterostructure is reached. These changes reflect the quality of the moiré structure in the examined areas in real space, i.e., moiré uniformity in terms of periodicity and amplitude.

Valuable information about the local orientation of the grown heterostructure is gained from polar profiles extracted from the  $\mu$ -LEED scan. They are shown in Figure 3(c) for an angular range of  $120^\circ$  (the diffraction patterns are 3-fold symmetric [26, 30]), where  $0^\circ$  corresponds to an alignment of the zig-zag direction of the hBN and dense packed rows of Ir(111). Focusing again on the right one of the two heterostructures in Figure 3(b), the moiré diffraction pattern of the hBN core exhibits two distinctive peaks, at  $0^\circ$  and  $60^\circ$ , where one peak is more intense than the other one, due to the two different atoms in the basis of the hBN lattice. When going in the step-down direction towards the heterostructure edge, the crystal structure exhibits several rotations as well as spot splitting, indicating that the transition from hBN to Gr is nontrivial, i.e., it contains hexagonal lattices of different orientation and composition. The maximum observed rotation of the moiré pattern with respect to the crystallographic orientation of the hBN lattice is  $\sim 20^\circ$ , which translates into real rotations of  $\lesssim 2^\circ$  when the magnifying property of the moiré is taken into account. We note that due to the nature of the moiré structure, its rotation and lattice parameter are interlinked. In particular,  $20^\circ$  rotation could cause up to  $\sim 6\%$  lattice parameter increase, which is insufficient to account for our observations (15% lattice parameter increase) described in the preceding paragraph. In the Ir step-up direction, the boundary between hBN and Gr is sharper and does not show obvious signs of alloying [see Figure 1 or Figure 3(b)]. However, a detailed analysis presented in Figure 3 points to the existence of a narrow alloy region in the vicinity of the hBN-Gr boundary. The moiré  $k$ -value shifts from  $k_{m,hBN}$  to  $k_{m,Gr}$ , and also similar relative lattice rotations up to  $\sim 2^\circ$  are found.

## B. Microstructuring via hBN Disintegration

If desired, hBN-Gr heterostructures with a narrow hBCN belt surrounding an hBN core can be synthesized through a short ethylene CVD step, in a similar way as has been done on other substrates [15, 31]. An example is shown in Figure 4(a) for a synthesis at 1170 K where the borazine has been dosed at  $10^{-8}$  mbar for 129 s and ethylene at  $2 \times 10^{-8}$  mbar for 58 s, resulting in two isolated heterostructures  $H_a$  and  $H_b$ . Then the heterostructures were subsequently heated up to 1370 K at a rate of  $\sim 1.5$  K/s, and the temperature was kept at that value for several minutes. During the entire heating and

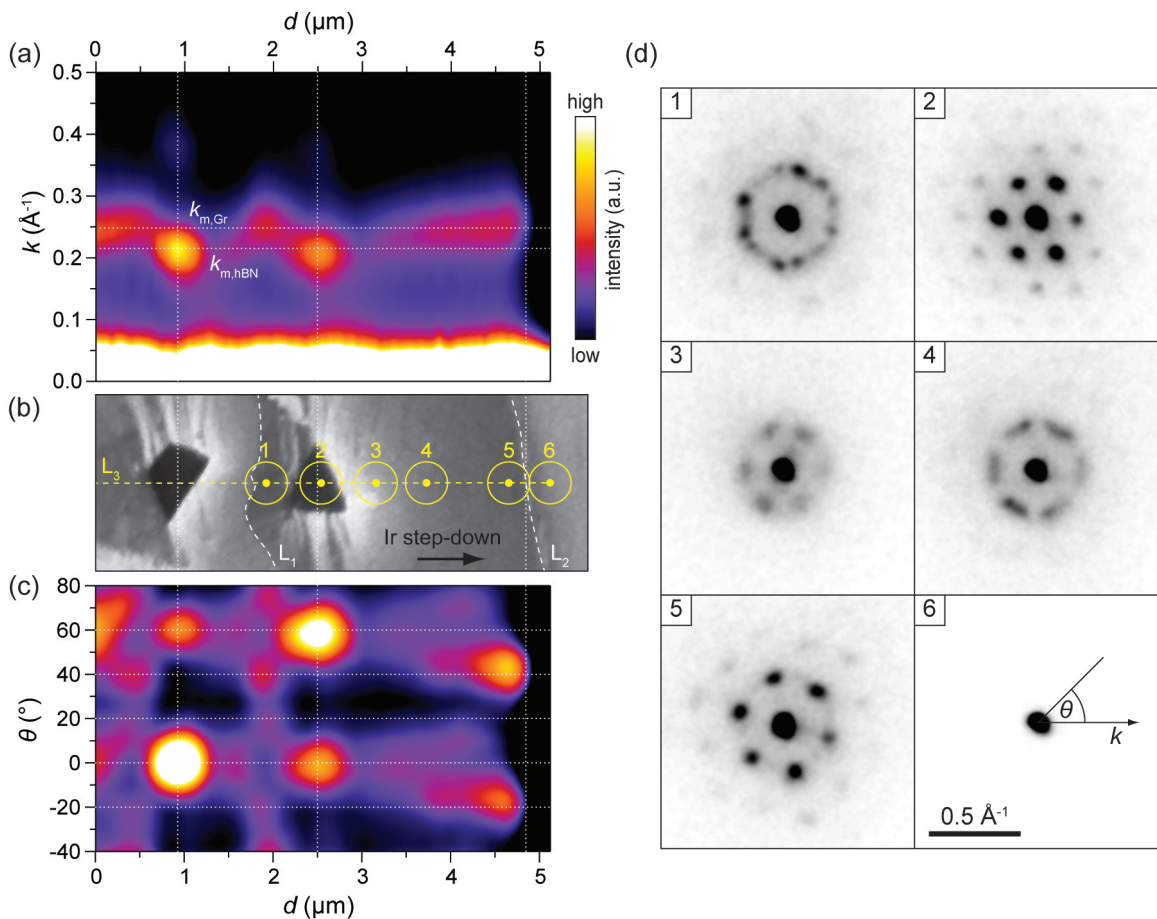


Figure 3. Analysis of hBN-Gr heterostructures with  $\mu$ -LEED. Analyzed area of the sample is shown in panel (b). Line  $L_1$  marks the border between the two coalesced heterostructures, line  $L_2$  marks the edge of a heterostructure towards Ir, and line  $L_3$  marks the path of the  $\mu$ -LEED scan. Yellow circles designate characteristic areas whose diffraction patterns are shown in panel (d) [only vicinity of the (0, 0) spot is shown]. Panels (a) and (c) show spatially-dependent radial average and polar profile of the of  $\mu$ -LEED patterns. Spatial coordinates of panels (a), (b) and (c) are aligned.  $E = 9.2$  eV in LEEM,  $E = 35.5$  eV in LEED.

annealing process, the heterostructures  $H_a$  and  $H_b$  were being imaged with LEEM (see Supplementary Movie 3). Due to significant decomposition at temperatures higher than  $\sim 1220$  K [26, 29, 32], hBN embedded within the heterostructures starts disintegrating as shown in Figure 4(b). The dominant locations for initiation of disintegration are boundaries between hBN and hBCN, which can be linked to the fact that interaction of the heterostructure with the Ir substrate is stronger there [14]. As the sample is kept at high temperature, disintegration continues exclusively at the free hBN edge that is not in contact with the rest of the heterostructure [Figure 4(c)], and eventually results in a complete removal of the hBN from the heterostructure [Figure 4(d)]. In this process, the surrounding material remains intact (at least on the scales accessible to LEEM), and the final result are hollow 2D microstructures of hBCN and Gr. Additional evidence for complete removal of hBN core is found in PEEM measurements, in which only the remaining microstructures are visible due to the reduction of the work

function (see Supplementary Figure S1). Size and lateral “thickness” of these microstructures depend on the size of the initial hBN cores and the lateral extension of the surrounding hBCN. Since hBN grows on Ir either as triangular or trapezoidal islands, the shape of Gr and hBCN microstructures is limited to a certain extent. However, subsequent oxygen etching of microstructures as well as their additional growth by ethylene CVD provides routes for further modification of their shape and size (an example will be given further below).

Additional insight into disintegration of hBN cores during microstructuring is obtained by monitoring their area ( $A$ ). The resulting data is plotted in Figure 5(a) as red circles for the two heterostructures  $H_a$  and  $H_b$  shown in Figure 4. The disintegration speed is relatively low in the beginning, but increases with time until the hBN vanishes from the sample surface completely. Apart from the different initial hBN core size, the data from  $H_a$  (triangular core) and  $H_b$  (trapezoidal core) looks similar, indicating that both hBN orientations present on Ir(111) disinte-

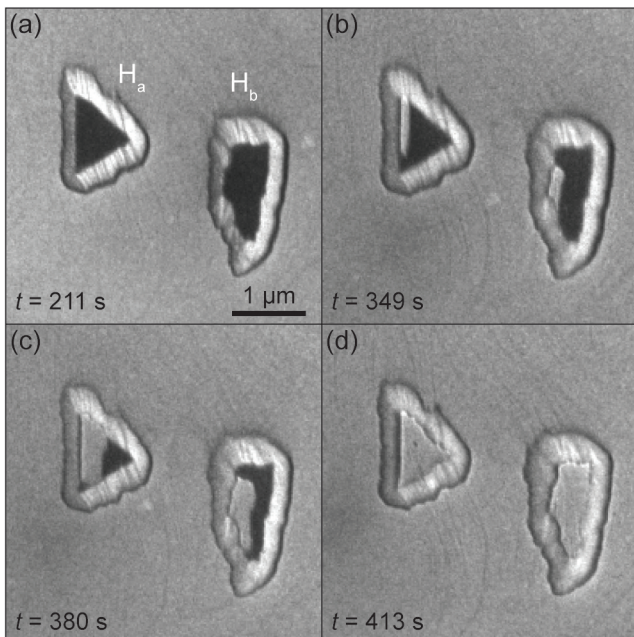


Figure 4. Formation of hollow 2D microstructures via hBN disintegration at high temperatures. (a) Well-defined hBN-Gr heterostructures  $H_a$  and  $H_b$  are synthesized at 1170 K. (b)-(d) Annealing of heterostructures at 1370 K results in disintegration of hBN, while leaving the surrounding hBCN and Gr intact. Time relative to the beginning of the borazine dosing is indicated in each panel.  $E = 9$  eV.

grate in the same manner. We propose the following model to describe the observed process.

Decomposition of hBN starts at the hBN-hBCN boundary, and further on at the free hBN edge. Hence, to a first approximation and with the aim of establishing a simplistic model, the decomposition rate is proportional to the hBN area (the first term on the right hand side of Equation 1) and becomes less significant as the time progresses. However, this rate alone cannot explain the increasing disintegration rate of hBN with time. That is why we introduce the second component of the decomposition rate (the second term on the right hand side of Equation 1) that relates to the local concentration of the adsorbates as follows. If we take hBN-Gr heterostructure with a partially decomposed hBN core, there will be a certain amount of the adsorbed species (arising from decomposition) trapped in the region bound by the remaining hBN and hBCN [see dark dots in Figure 5(b)]. As hBN decomposes further, the space available to these species increases and their concentration decreases accordingly, especially when taking into account desorption of B and N from the surface and possible dissolution of B atoms in Ir at high temperatures [33]. Due to the decrease of adsorbates concentration, the system is constantly pushed into a non-equilibrium state, and decomposition of hBN is further accelerated [34]. Therefore, the second component of the hBN decomposition rate is proportional to the area of already disintegrated

hBN, and becomes relevant only after an initial portion of hBN has already been removed from the surface. The reduction of hBN area  $A$  can then be written as

$$\frac{dA}{dt} = -s_1 A - s_2 (A_0 - A) \quad (1)$$

where  $A_0$  is the area of hBN core prior to its decomposition [ $A_0 = A(t = 0)$ ]. The solution to the above equation is

$$A(t) = \frac{A_0}{s_2 - s_1} \left[ s_2 - s_1 e^{(s_2 - s_1)t} \right]. \quad (2)$$

Equation 2 can be used to fit the data from Figure 5(a) and calculate the values of  $s_1$  and  $s_2$ . For the heterostructure  $H_a$ , we obtain  $s_1 = 0.001 \text{ s}^{-1}$  and  $s_2 = 0.025 \text{ s}^{-1}$ , and for the heterostructure  $H_b$  we get  $s_1 = 0.001 \text{ s}^{-1}$  and  $s_2 = 0.024 \text{ s}^{-1}$ . Therefore, the decomposition rate linked to  $s_1$  is an order of magnitude smaller than the one linked to  $s_2$ , but it is essential in the initial stages of the decomposition process. Overall, the values of  $s_1$  and  $s_2$  for  $H_a$  and  $H_b$  are practically identical, indicating generality of processes governing the hBN decomposition.

A LEEM image of a larger area containing several microstructures is shown in Figure 6(a), where the electron energy is chosen to emphasize the shape of the microstructures. As before, triangular and trapezoidal microstructures are visible. Also, an example of two merged structures is found close to the center of the field of view. If the heterostructure annealing step is performed at 1470 K instead of 1370 K, partial degradation of Gr and hBCN can also take place. Apparently, at this temperature sufficient non-equilibrium conditions of the hBCN material and the surrounding adsorbed species [see bright dots in Figure 5(b)] can be reached, and significant number of B, C and N atoms can detach from the hBNC crystal (atom detachment rate becomes much larger than adsorbate attachment rate). As a result, not only hollow but also concave Gr and hBCN microstructures can be found on the Ir surface. If the size of the initial hBN core is sufficiently large and its edges are straight enough, Gr and hBCN microstripes can be fabricated. One such stripe is shown in Figure 6(b). Similar as in the case of hollow microstructures, the thickness of the stripe can be further modified by applying oxygen etching (thinning) or CVD of ethylene (thickening), since both of these processes take place at the edges of the existing Gr and hBCN structures. An example of thinning is given in Figure 6(c) where an hBCN stripe has been thinned down by etching in oxygen at 1170 K and a pressure of  $2.5 \times 10^{-8}$  mbar. The stripe is thinned from  $0.36 \text{ μm}$  to  $0.2 \text{ μm}$  during 418 s, yielding the average thinning speed of  $\sim 0.4 \text{ nm/s}$ .

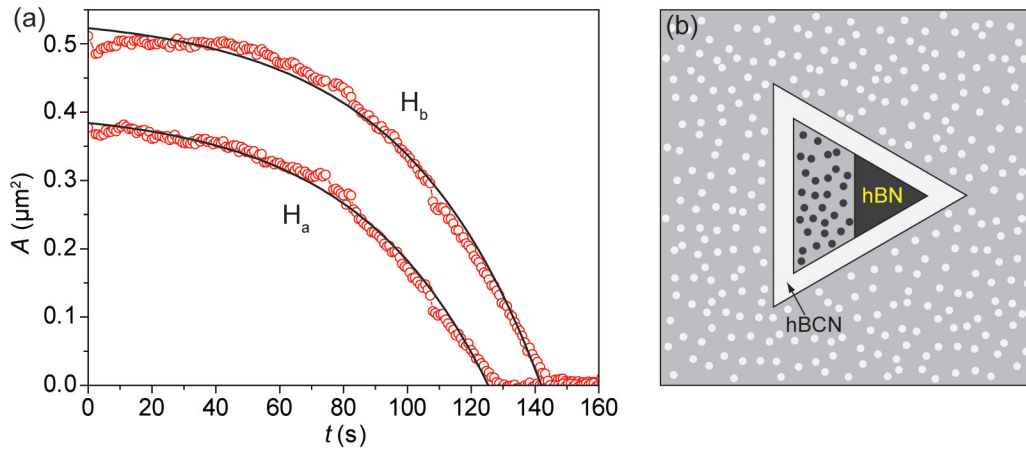


Figure 5. (a) Red circles correspond to the area of the hBN cores of the heterostructures  $H_a$  and  $H_b$  shown in Figure 4 as a function of annealing duration at 1370 K. Black lines are fits to the decay model given by Equations 1 and 2. (b) Illustration of a partially decomposed heterostructure, with the in-equilibrium adsorbate species surrounding hBCN region (bright dots) and the out-of-equilibrium species trapped inside the forming microstructure (dark dots).

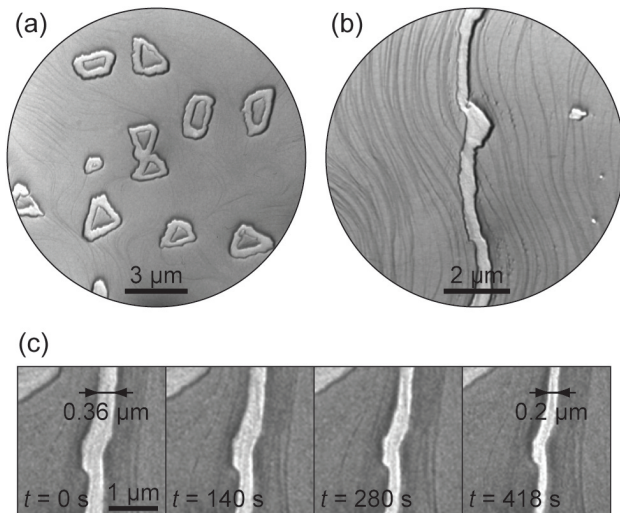


Figure 6. Microstructures obtained by disintegration of hBN. (a) Various hollow structures (synthesis at 1170 K, annealing at 1370 K) and (b) elongated stripe (synthesis at 1370 K, annealing at 1480 K). (c) An example of a stripe thinning process via oxygen etching.  $E = 5$  eV.

#### IV. DISCUSSION

In sequential CVD of borazine and ethylene, C monomers and small C clusters, originating from ethylene decomposition [35, 36], are mixing with the adsorbed species that remain on the Ir surface after hBN growth, as evident from Figure 1(e). These species exist since islands of 2DMs must be in equilibrium with the surrounding adatom or cluster gas (which serves as a feedstock during growth) in order to be stable at a given temperature [27, 34, 35]. Therefore, possible candidates for the mixing with C are B atoms, N atoms or various borazine fragments (either isolated or already ar-

ranged in small hBN clusters). N atoms (including the ones forming various molecules), B atoms and borazine molecules desorb from the Ir(111) at temperatures relevant for our experiments, as was shown in temperature programmed desorption (TPD) and x-ray photoemission spectroscopy (XPS) experiments [37–39]. One additional source of mixing could be B atoms dissolved into the subsurface region of Ir [26, 32], but their contribution must be minor since the alloy formation shows an obvious dependence on the surface morphology of Ir (alloying in the step-down direction is more pronounced), thus confirming the relevance of species present on the surface.

This leaves dehydrogenated borazine fragments  $B_xN_y$  and small hBN clusters as the most abundant species mixing with C during heterostructure growth and formation of hBCN alloy. The C:(B,N) ratio increases away from the hBN edge as the  $B_xN_y$  fragments are incorporated into the growing heterostructure and become depleted. Consequently, far enough from the hBN core, hBCN becomes Gr, as is evident from the  $\mu$ -LEED analysis presented in Figure 3. Spatial variation of the C:(B,N) ratio also affects the electronic structure of the hBCN alloy as visible in PEEM (see Supplementary Figure S1), where variations in work function [21] can provide spatially-dependent photoemission yield. LEEM data [Figure 1(a)-(d)] clearly demonstrates successful incorporation of the  $B_xN_y$  fragments into the growing hBCN alloy in the step-down direction of the Ir surface. This is analogous to the growth of 2DMs on metal substrates that is often more effective or even exclusive in the step-down direction [35, 40, 41]. Accordingly, we speculate that the reason for anisotropic alloying can be strong binding of hBN island edges to Ir step edges, which hinders attachment of  $B_xN_y$  fragments to the growing heterostructure in the step-up direction of Ir. This is, however, not valid for carbon species that are incorporated into the heterostructure also in the step-up direc-

tion, which is a clear indication of different growth mechanisms of hBCN alloy and graphene regions. Also, pronounced anisotropy in diffusion of the  $B_xN_y$  fragments and small hBN clusters (differences in step-up, step-down and along-the-terrace diffusion) might cause local inhomogeneities in material supply, and contribute to the alloy non-uniformity and appearance of distinct graphene regions within the hBCN alloy [see white arrow in Figure 1(d)]. Overall, isotropic alloying could be achieved if more advanced methods for substrate preparation would be employed (that would result in low density of surface steps), which leaves room for further advancement in the material quality.

Moiré diffraction spots are always visible in  $\mu$ -LEED analysis (see Figure 3), proving that besides pure hBN and Gr regions, hBCN alloy also exhibits a hexagonal lattice. We do not observe simultaneous presence of the hBN and Gr moiré spots, which indicates that indeed the transition region from hBN to Gr is a locally homogeneous alloy. However, it is possible that separated hBN and Gr nano-domains, too small to provide a clear diffraction pattern, exist within hBCN, since calculations predict that phase segregation is energetically favorable [18–21]. It can be inferred from Figure 3(a) that the lattice constant of hBCN alloy changes from almost 2.48 Å [29] [lattice constant of hBN on Ir(111)] to 2.45 Å [28] [lattice constant of Gr on Ir(111)] as a function of the distance from the hBN edge. In a recent  $\mu$ -LEED study, Camilli et al. find that the hBCN alloy has a lattice constant of 2.57 Å when analyzing more complex samples consisting of Gr nanodots embedded in an hBCN matrix [42]. This suggests that different synthesis procedures can provide hBCN alloys of different stoichiometries and lattice constants. Modification of lattice constant in our experiments is accompanied by the in-plane rotations across the heterostructure, which we ascribe to lattice-matching process arising from the continuous variation of the hBCN lattice constant. Similar lattice miss-orientations were found in Gr-hBN heterostructure synthesis on Cu foils by atmospheric pressure CVD [31].

During the decomposition of hBN and microstructuring, N atoms desorb from the surface, most probably forming various molecules since N is volatile. B atoms, especially at temperatures above  $\approx 1220$  K, can diffuse into the subsurface regions of the Ir, they segregate to the surface after the sample is cooled, and are then easily detected with LEEM [26]. But since no significant segregation of B has been observed during cooldown, we conclude that a large portion of B atoms also desorbs from the Ir surface at high annealing temperatures. In addition, if the temperature increase is rapid as in our experiments, the time available to B atoms to dissolve into Ir, before they have enough energy to desorb from the surface, is limited. This further supports our model of hBN decomposition, which depends on the concentration of adsorbates on the Ir surface. The hBN-Gr het-

erostructures and the corresponding microstructures are isolated from each other and are not mutually interconnected or overlapped, and are therefore suitable for further integration into more complex systems. It is worth noting that a few other studies also reported on the fabrication of hollow 2D structures on Pt and Cu foils by growth-etching procedures in atmospheric-pressure tube furnaces, namely hexagonal Gr rings [43, 44] and triangular hBN structures [45].

## V. CONCLUSION

In sequential CVD growth of lateral hBN-Gr heterostructures on Ir(111), a 2D hexagonal alloy consisting of B, C, and N (hBCN) is formed at the interface between hBN and Gr. Alloying occurs because in the first synthesis step epitaxial hBN islands are formed that are in equilibrium with the surrounding borazine fragments, and these fragments mix with C species that originate from ethylene decomposition taking place in the second synthesis step. The C:(B,N) ratio within the alloy, as well as the width of the alloy region, can be modified by altering the temperature and the ethylene pressure during synthesis. In this way, it is possible to tune the electronic properties (i.e., the band gap and the work function) and spatial arrangement of the alloyed material, which provides means for customization that is crucial in many applications. In addition, introduction of oxygen into the synthesis procedure enables production of sharp hBN-Gr interfaces without the hBCN region. Due to the decomposition of hBN at elevated temperatures, it is possible to fabricate various hBCN and Gr microstructures upon annealing of hBN-Gr heterostructures. This kind of hBN-templating, in combination with well-known transfer techniques, effectively provides foundations of a new method for production of micro- and nano-sized conducting and semiconducting elements that can be integrated in more complex devices (e.g. transistors, solar cells, light emitters or resonators). The advantage of this method over more established ones, e.g., lithography, is that it does not require undesirable ex situ manipulation of the sensitive atomic layers, structures in the 100 nm range can be produced with ease, and hence we envision its further development as an alternative route for technological implementation of 2DMs.

## VI. ACKNOWLEDGMENTS

M.P. would like to thank the Alexander von Humboldt Foundation for financial support.

## VII. REFERENCES



- [1] K. S. Novoselov, A. Mishchenko, A. Carvalho, A. H. Castro Neto, 2D materials and van der Waals heterostructures, *Science* 353 (6298) (2016) aac9439. doi:10.1126/science.aac9439.
- [2] C. R. Dean, A. F. Young, I. Meric, C. Lee, L. Wang, S. Sorgenfrei, K. Watanabe, T. Taniguchi, P. Kim, K. L. Shepard, J. Hone, Boron nitride substrates for high-quality graphene electronics, *Nat. Nanotechnol.* 5 (10) (2010) 722–726. doi:10.1038/nnano.2010.172.
- [3] J. S. Ross, P. Klement, A. M. Jones, N. J. Ghimire, J. Yan, D. G. Mandrus, T. Taniguchi, K. Watanabe, K. Kitamura, W. Yao, D. H. Cobden, X. Xu, Electrically tunable excitonic light-emitting diodes based on monolayer WSe<sub>2</sub> p-n junctions, *Nat. Nanotechnol.* 9 (4) (2014) 268–272. doi:10.1038/nnano.2014.26.
- [4] L. Britnell, R. M. Ribeiro, A. Eckmann, R. Jalil, B. D. Belle, A. Mishchenko, Y.-J. Kim, R. V. Gorbachev, T. Georgiou, S. V. Morozov, A. N. Grigorenko, A. K. Geim, C. Casiraghi, A. H. C. Neto, K. S. Novoselov, Strong Light-Matter Interactions in Heterostructures of Atomically Thin Films, *Science* 340 (6138) (2013) 1311–1314. doi:10.1126/science.1235547.
- [5] X. Duan, C. Wang, J. C. Shaw, R. Cheng, Y. Chen, H. Li, X. Wu, Y. Tang, Q. Zhang, A. Pan, J. Jiang, R. Yu, Y. Huang, X. Duan, Lateral epitaxial growth of two-dimensional layered semiconductor heterojunctions, *Nat. Nanotechnol.* 9 (12) (2014) 1024–1030. doi:10.1038/nnano.2014.222.
- [6] L. Ci, L. Song, C. Jin, D. Jariwala, D. Wu, Y. Li, A. Srivastava, Z. F. Wang, K. Storr, L. Balicas, F. Liu, P. M. Ajayan, Atomic layers of hybridized boron nitride and graphene domains, *Nat. Mater.* 9 (5) (2010) 430–435. doi:10.1038/nmat2711.
- [7] K. I. Bolotin, K. J. Sikes, J. Hone, H. L. Stormer, P. Kim, Temperature-dependent transport in suspended graphene, *Phys. Rev. Lett.* 101 (9) (2008) 096802. doi:10.1103/PhysRevLett.101.096802.
- [8] G. Cassabois, P. Valvin, B. Gil, Hexagonal boron nitride is an indirect bandgap semiconductor, *Nat. Photonics* 10 (4) (2015) 262–266. doi:10.1038/nphoton.2015.277.
- [9] M. P. Levendorf, C.-J. Kim, L. Brown, P. Y. Huang, R. W. Havener, D. A. Muller, J. Park, Graphene and boron nitride lateral heterostructures for atomically thin circuitry, *Nature* 488 (7413) (2012) 627–632. doi:10.1038/nature11408.
- [10] Z. Liu, L. Ma, G. Shi, W. Zhou, Y. Gong, S. Lei, X. Yang, J. Zhang, J. Yu, K. P. Hackenberg, A. Babakhani, J.-C. Idrobo, R. Vajtai, J. Lou, P. M. Ajayan, In-plane heterostructures of graphene and hexagonal boron nitride with controlled domain sizes, *Nat. Nanotechnol.* 8 (2) (2013) 119–124. doi:10.1038/nnano.2012.256.
- [11] Y. Gong, G. Shi, Z. Zhang, W. Zhou, J. Jung, W. Gao, L. Ma, Y. Yang, S. Yang, G. You, R. Vajtai, Q. Xu, A. H. MacDonald, B. I. Yakobson, J. Lou, Z. Liu, P. M. Ajayan, Direct chemical conversion of graphene to boron- and nitrogen- and carbon-containing atomic layers, *Nat. Commun.* 5 (2014) 3193. doi:10.1038/ncomms4193.
- [12] P. Sutter, R. Cortes, J. Lahiri, E. Sutter, Interface formation in monolayer graphene-boron nitride heterostructures, *Nano Lett.* 12 (9) (2012) 4869–4874. doi:10.1021/nl302398m.
- [13] Y. Gao, Y. Zhang, P. Chen, Y. Li, M. Liu, T. Gao, D. Ma, Y. Chen, Z. Cheng, X. Qiu, W. Duan, Z. Liu, Toward single-layer uniform hexagonal boron nitride-graphene patchworks with zigzag linking edges, *Nano Lett.* 13 (7) (2013) 3439–3443. doi:10.1021/nl4021123.
- [14] M. Liu, Y. Li, P. Chen, J. Sun, D. Ma, Q. Li, T. Gao, Y. Gao, Z. Cheng, X. Qiu, Y. Fang, Y. Zhang, Z. Liu, Quasi-freestanding monolayer heterostructure of graphene and hexagonal boron nitride on Ir(111) with a zigzag boundary, *Nano Lett.* 14 (11) (2014) 6342–6347. doi:10.1021/nl502780u.
- [15] P. Sutter, Y. Huang, E. Sutter, Nanoscale integration of two-dimensional materials by lateral heteroepitaxy, *Nano Lett.* 14 (8) (2014) 4846–4851. doi:10.1021/nl502110q.
- [16] R. Drost, S. Kezilebieke, M. M. Ervasti, S. K. Hämäläinen, F. Schulz, A. Harju, P. Liljeroth, Synthesis of Extended Atomically Perfect Zigzag Graphene - Boron Nitride Interfaces, *Sci. Rep.* 5 (1) (2015) 16741. doi:10.1038/srep16741.
- [17] T. Gao, X. Song, H. Du, Y. Nie, Y. Chen, Q. Ji, J. Sun, Y. Yang, Y. Zhang, Z. Liu, Temperature-triggered chemical switching growth of in-plane and vertically stacked graphene-boron nitride heterostructures, *Nat. Commun.* 6 (2015) 6835. doi:10.1038/ncomms7835.
- [18] K. T. Lam, Y. Lu, Y. P. Feng, G. Liang, Stability and electronic structure of two dimensional C<sub>x</sub>(BN)<sub>y</sub> compound, *Appl. Phys. Lett.* 98 (2) (2011) 96–99. doi:10.1063/1.3535604.
- [19] J. da Rocha Martins, H. Chacham, Disorder and Segregation in B-C-N Graphene-Type Layers and Nanotubes: Tuning the Band Gap, *ACS Nano* 5 (1) (2011) 385–393. doi:10.1021/nn101809j.
- [20] A. K. Manna, S. K. Pati, Tunable Electronic and Magnetic Properties in B<sub>x</sub>N<sub>y</sub>C<sub>z</sub> Nanohybrids: Effect of Domain Segregation, *The Journal of Physical Chemistry C* 115 (21) (2011) 10842–10850. doi:10.1021/jp202195b.
- [21] Y. Xie, H. Yu, H. Zhang, H. Fu, Tuning the band gaps and work functions via topology and carbon concentration: a first-principles investigation of C<sub>x</sub>(BN)<sub>y</sub> compounds, *Phys. Chem. Chem. Phys.* 14 (13) (2012) 4391. doi:10.1039/c2cp23964g.
- [22] M. Zhang, G. Gao, A. Kutana, Y. Wang, X. Zou, J. S. Tse, B. I. Yakobson, H. Li, H. Liu, Y. Ma, Two-dimensional boron-nitrogen-carbon monolayers with tunable direct band gaps, *Nanoscale* 7 (28) (2015) 12023–12029. doi:10.1039/C5NR03344F.
- [23] M. O. Watanabe, S. Itoh, T. Sasaki, K. Mizushima, Visible-Light-Emitting Layered BC<sub>2</sub>N Semiconductor, *Phys. Rev. Lett.* 77 (1) (1996) 187–189. doi:10.1103/PhysRevLett.77.187.
- [24] J. Lu, K. Zhang, X. Feng Liu, H. Zhang, T. Chien Sum, A. H. Castro Neto, K. P. Loh, Order-disorder transition in a two-dimensional boron-carbon-nitride alloy, *Nat. Commun.* 4 (May) (2013) 2681. doi:10.1038/ncomms3681.
- [25] M. Petrović, J. T. Sadowski, A. Šiber, M. Kralj, Wrinkles of graphene on Ir(111): Macroscopic network ordering and internal multi-lobed structure, *Carbon* 94 (2015) 856–863. doi:10.1016/j.carbon.2015.07.059.
- [26] M. Petrović, U. Hagemann, M. Horn-von Hoegen, F. J. Meyer zu Heringdorf, Microanalysis of single-layer hexag-

- onal boron nitride islands on Ir(111), *Appl. Surf. Sci.* 420 (2017) 504–510. doi:10.1016/j.apsusc.2017.05.155.
- [27] E. Loginova, N. C. Bartelt, P. J. Feibelman, K. F. McCarty, Evidence for graphene growth by C cluster attachment, *New J. Phys.* 10 (0001) (2008) 093026. doi:10.1088/1367-2630/10/9/093026.
- [28] A. T. N'Diaye, J. Coraux, T. N. Plasa, C. Busse, T. Michely, Structure of epitaxial graphene on Ir(111), *New J. Phys.* 10 (111) (2008) 043033. doi:10.1088/1367-2630/10/4/043033.
- [29] F. H. Farwick Zum Hagen, D. M. Zimmermann, C. C. Silva, C. Schlueter, N. Atodiressei, W. Jolie, A. J. Martnez-Galera, D. Dombrowski, U. A. Schröder, M. Will, P. Lazi, V. Caciuc, S. Bligel, T. L. Lee, T. Michely, C. Busse, Structure and Growth of Hexagonal Boron Nitride on Ir(111), *ACS Nano* 10 (12) (2016) 11012–11026. doi:10.1021/acs.nano.6b05819.
- [30] F. Orlando, P. Lacovig, L. Omiciuolo, N. G. Apostol, R. Larciprete, A. Baraldi, S. Lizzit, Epitaxial growth of a single-domain hexagonal boron nitride monolayer, *ACS Nano* 8 (12) (2014) 12063–12070. doi:10.1021/nm5058968.
- [31] G. H. Han, J. A. Rodríguez-Manzo, C. W. Lee, N. J. Kybert, M. B. Lerner, Z. J. Qi, E. N. Dattoli, A. M. Rappe, M. Drndic, A. T. Johnson, Continuous growth of hexagonal graphene and boron nitride in-plane heterostructures by atmospheric pressure chemical vapor deposition, *ACS Nano* 7 (11) (2013) 10129–10138. doi:10.1021/nm404331f.
- [32] D. Usachov, A. Fedorov, O. Vilkov, V. K. Adamchuk, L. V. Yashina, L. Bondarenko, A. A. Saranin, A. Grüneis, D. V. Vyalikh, Experimental and computational insight into the properties of the lattice-mismatched structures: Monolayers of h-BN and graphene on Ir(111), *Phys. Rev. B* 86 (15) (2012) 155151. doi:10.1103/PhysRevB.86.155151.
- [33] I. Zeiringer, X. Cheng, X.-Q. Chen, E. Bauer, G. Giester, P. F. Rogl, Crystal structures and constitution of the binary system iridium-boron, *Sci. China Mater.* 58 (8) (2015) 649–668. doi:10.1007/s40843-015-0078-6.
- [34] P. C. Rogge, K. Thürmer, M. E. Foster, K. F. McCarty, O. D. Dubon, N. C. Bartelt, Real-time observation of epitaxial graphene domain reorientation., *Nat. Commun.* 6 (2015) 6880. doi:10.1038/ncomms7880.
- [35] E. Loginova, N. C. Bartelt, P. J. Feibelmarr, K. F. McCarty, Factors influencing graphene growth on metal surfaces, *New J. Phys.* 11 (2009) 063046. doi:10.1088/1367-2630/11/6/063046.
- [36] H. Tetlow, J. Posthuma de Boer, I. J. Ford, D. D. Vvedensky, D. Curcio, L. Omiciuolo, S. Lizzit, A. Baraldi, L. Kantorovich, Ethylene decomposition on Ir(111): initial path to graphene formation, *Phys. Chem. Chem. Phys.* 18 (40) (2016) 27897–27909. doi:10.1039/C6CP03638D.
- [37] J. C. Cornish, N. R. Avery, Adsorption of N<sub>2</sub>, O<sub>2</sub>, N<sub>2</sub>O and NO on Ir(111) by EELS and TPD, *Surf. Sci.* 235 (2-3) (1990) 209–216. doi:10.1016/0039-6028(90)90795-A.
- [38] C. Weststrate, J. Bakker, a.C. Gluhoi, W. Ludwig, B. Nieuwenhuys, Ammonia oxidation on Ir(111): Why Ir is more selective to N<sub>2</sub> than Pt, *Catal. Today* 154 (1-2) (2010) 46–52. doi:10.1016/j.cattod.2010.03.049.
- [39] F. Orlando, R. Larciprete, P. Lacovig, I. Boscarato, A. Baraldi, S. Lizzit, Epitaxial Growth of Hexagonal Boron Nitride on Ir(111), *J. Phys. Chem. C* 116 (1) (2012) 157–164. doi:10.1021/jp207571n.
- [40] P. W. Sutter, J.-I. Flege, E. A. Sutter, Epitaxial graphene on ruthenium, *Nat. Mater.* 7 (5) (2008) 406–411. doi:10.1038/nmat2166.
- [41] P. Sutter, J. Lahiri, P. Albrecht, E. Sutter, Chemical vapor deposition and etching of high-quality monolayer hexagonal boron nitride films, *ACS Nano* 5 (9) (2011) 7303–7309. doi:10.1021/nm202141k.
- [42] L. Camilli, J. H. Jørgensen, J. Tersoff, A. C. Stoot, R. Balog, A. Cassidy, J. T. Sadowski, P. Bøggild, L. Hornekær, Self-assembly of ordered graphene nanodot arrays, *Nat. Commun.* 8 (1) (2017) 47. doi:10.1038/s41467-017-00042-4.
- [43] T. Ma, W. Ren, X. Zhang, Z. Liu, Y. Gao, L.-C. Yin, X.-L. Ma, F. Ding, H.-M. Cheng, Edge-controlled growth and kinetics of single-crystal graphene domains by chemical vapor deposition., *Proc. Natl. Acad. Sci. U.S.A.* 110 (51) (2013) 20386–91. doi:10.1073/pnas.1312802110.
- [44] J. Liu, Y. Xu, H. Cai, C. Zuo, Z. Huang, L. Lin, X. Guo, Z. Chen, F. Lai, Double hexagonal graphene ring synthesized using a growth-etching method, *Nanoscale* 8 (2016) 14178–14183. doi:10.1039/C6NR02515C.
- [45] S. Sharma, G. Kalita, R. Vishwakarma, Z. Zulkiffi, M. Tanemura, Opening of triangular hole in triangular-shaped chemical vapor deposited hexagonal boron nitride crystal, *Sci. Rep.* 5 (1) (2015) 10426. doi:10.1038/srep10426.